Observation and laser spectroscopy of ytterbium monomethoxide, YbOCH₃

Benjamin L. Augenbraun [1,2,*] Zack D. Lasner,[1,2] Alexander Frenett,[1,2] Hiromitsu Sawaoka,[1,2] Anh T. Le [3]
John M. Doyle,[1,2] and Timothy C. Steimle[3,†]

[1]*Department of Physics, Harvard University, Cambridge, Massachusetts 02138, USA*
[2]*Harvard-MIT Center for Ultracold Atoms, Cambridge, Massachusetts 02138, USA*
[3]*School of Molecular Science, Arizona State University, Tempe, Arizona 85287, USA*

We describe a laser spectroscopic study of ytterbium monomethoxide, YbOCH₃, a species of interest to searches for time-reversal symmetry violation using laser-cooled molecules. We report measurements of vibrational structure in the $\tilde{X}$ and $\tilde{A}$ states, vibrational branching ratios for several components of the $\tilde{A}$ state, and radiative lifetimes of low-lying electronic states. *Ab initio* calculations are used to aid the assignment of vibronic emission bands and provide insight into the electronic and vibrational structure. Our results demonstrate that rapid optical cycling is feasible for YbOCH₃, opening a path to orders-of-magnitude increased sensitivity in future measurements of *P*- and/or *T*-violating physics.

I. INTRODUCTION

Precision measurements of symmetry-violating electromagnetic moments provide stringent tests of physics beyond the standard model (BSM) [1–6]. Polar molecules containing a high-*Z* nucleus have emerged as ideal probes because they may combine intrinsic sensitivity to CP-violating moments with structural features that aid high-precision experiments [4,7–10]. For example, experiments using a variety of (diatomic) polar molecules have set increasingly tight limits on the value of an electron electric dipole moment (eEDM), ultimately constraining CP-violating BSM physics at energy scales $\gtrsim$10 TeV [10–13]. Molecules with enhanced sensitivity to a nuclear magnetic quadrupole moment (nMQM) have been proposed for similar tests [14,15]. Concurrent with these advances in precision measurement, molecular laser cooling has recently been extended to both diatomic [16] and triatomic [17] species containing the heavy Yb nucleus. Measurements combining properly chosen molecular species with laser cooling to the μK regime are predicted to provide several orders of magnitude increased sensitivity to both the eEDM and the nMQM, potentially allowing experiments to probe PeV-scale BSM physics [18].

A number of laser-coolable molecules have been proposed for next-generation eEDM measurements, with linear species garnering the most attention due to their structural simplicity [16,18–22]. The degenerate vibrational bending mode in YbOH is a promising venue for future eEDM or nMQM measurements due to its small parity doublet, analogous to the Ω doublets that have allowed strong systematic error rejection in eEDM experiments [8,11–13,23]. The recent laser cooling of YbOH to $\ll$1 mK in one dimension represents an impor-

tant first step toward eEDM measurements with laser-cooled polyatomic molecules [17]. However, in YbOH the energy of the first bending excitation is relatively high ($\omega_2 \sim 330$ cm⁻¹) and anharmonic [24], limiting feasible coherence times to $\lesssim$800 ms [25].

By contrast, nonlinear symmetric top molecules possess long-lived parity-doubled states due to rigid body rotation about the molecular symmetry axis ("*K* doublets").[1] For instance, the $K'' = 1$ level in YbOCH₃ is expected to have a spontaneous lifetime much longer than 100 s due to its low energy ($\sim$10 cm⁻¹) and proton spin statistics. This could lead to $>$30× improved statistical sensitivity to BSM physics if full advantage were taken of the feasible coherence times. Moreover, the very small *K* doubling of metastable rotational levels enables full polarization and internal comagnetometry, two features that have enabled robust rejection of systematic errors in recent eEDM measurements [23,26]. To fully leverage the lifetime of the eEDM-sensitive *K* doublet in a neutral species requires cooling to ultracold temperatures. Laser cooling of molecules is a proven route toward this end [27–29]. Importantly, the recent one-dimensional laser cooling of CaOCH₃ to <1 mK shows that the complicated vibrational and rotational structure in symmetric top molecules does not adversely affect the laser-cooling process [30]. Ytterbium monomethoxide (YbOCH₃), isoelectronic to CaOCH₃, is thus an intriguing candidate for eEDM/nMQM measurements using laser-cooled molecules, but to our knowledge there are no previously reported observations of this species.

The alkaline-earth monomethoxides, *M*OCH₃ (*M* = Ca, Sr, Ba), have received considerable spectroscopic attention [31–37]. These molecules comprise an alkaline-earth atom

---

*augenbraun@g.harvard.edu
†TSteimle@asu.edu

[1]The quantum number *K* denotes the molecule-frame projection of *N*, the total angular momentum excluding spin. States with $|K| > 0$ are doubly degenerate. Note that, necessarily, $N \geqslant |K|$.
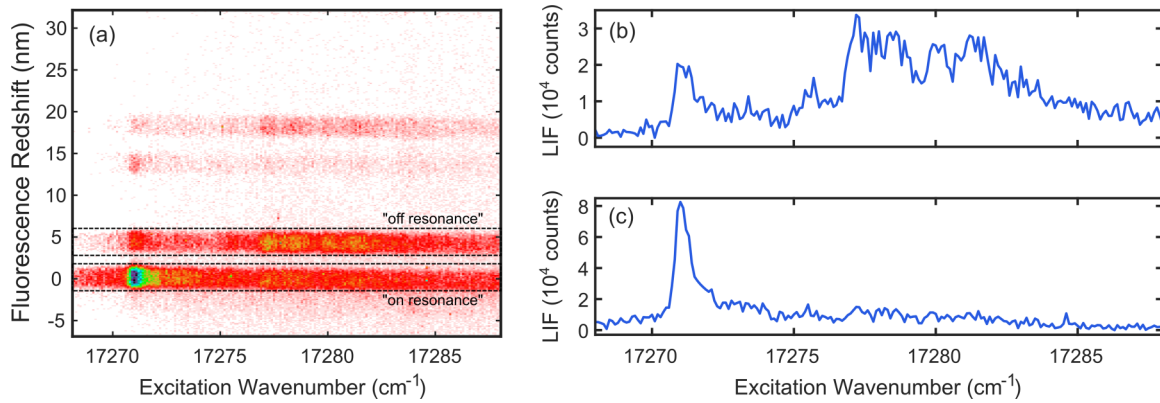
FIG. 1. (a) Pulsed-dye laser 2D spectrum in the vicinity of the YbOCH$_3$ $\tilde{A}\ ^2E_{1/2} \leftarrow \tilde{X}\ ^2A_1$ band head. Integration at fixed fluorescence wavelength can be used to obtain excitation spectra. Color scale indicates number of LIF counts detected. Integration at fixed excitation wave number would yield DLIF spectra, but we describe higher-resolution DLIF data below. (b) Excitation spectrum obtained by vertical integration in the region labeled "off-resonance." Strong decay to the bending mode is observed from approximately 10 cm^{-1} to the blue of the origin frequency (see text). (c) Excitation spectrum by vertical integration in the region labeled "on-resonance." A strong band head associated with the $0_0^0\ \tilde{A}\ ^2E_{1/2} \leftarrow \tilde{X}\ ^2A_1$ vibronic transition is observed, characteristic of a $^2E - ^2A_1$ transition.

ionically and monovalently bonded to a relatively electronegative methoxy ligand [38,39]. They have linear M-O-C backbones with three off-axis H atoms (C_{3v} symmetry) in both the ground ($\tilde{X}\ ^2A_1$) and low-lying excited ($\tilde{A}\ ^2E$ and $\tilde{B}\ ^2A_1$) states [37,40]. The unpaired valence electron is in a metal-centered, hybrid nonbonding orbital [35] resulting in "diagonal" vibrational branching ratios (VBRs) and short radiative lifetimes, properties highly favorable for laser cooling [41,42]. It is not *a priori* obvious that Yb-containing analogues will share all of these properties, e.g., due to previously observed perturbations in YbF and YbOH [24,43].

Here we present an initial experimental characterization of the previously unobserved lanthanide-containing symmetric top molecule YbOCH$_3$. This is, to date, the highest-mass neutral symmetric top molecule suitable for precision measurement experiments that has been experimentally characterized. An intense electronic transition near 579 nm has been detected and assigned to the origin band of an $\tilde{A}\ ^2E_{1/2} \leftarrow \tilde{X}\ ^2A_1$ electronic transition. Dispersed laser-induced fluorescence (DLIF) measurements for YbOCH$_3$ and the isotopologue YbOCD$_3$ are used to characterize the vibrational structure in the ground and excited electronic states. In addition, we have recorded a portion of the high-resolution spectrum of the $0_0^0\ \tilde{A}\ ^2E_{1/2} \leftarrow \tilde{X}\ ^2A_1$ band. We complement these measurements with *ab initio* electronic structure calculations and find excellent agreement between theory and experiment. Finally, we discuss the prospects for direct laser cooling of YbOCH$_3$ and its use in future precision measurements.

II. EXPERIMENTAL SETUP

Molecular beams of YbOCH$_3$ are produced in a setup similar to that used in recent studies of YbOH [22,24,44]. Briefly, a rotating ytterbium rod is ablated at ∼20 Hz with a short pulse of 532-nm radiation (∼10 ns, ∼5 mJ). The ablation plume is entrained in and reacted with a gas mixture of methanol vapor and Ar in a supersonic expansion. The gas mixture is produced by passing Ar at ∼4000 kPa over room-temperature liquid methanol (CH$_3$OH; vapor pressure

∼10 kPa). Typical pulse widths for the molecular beam are ∼50 μs. We use a number of complementary spectroscopic methods, including two-dimensional (2D) spectroscopy, DLIF spectroscopy, radiative decay, and high-resolution excitation spectroscopy to conclusively confirm detection of YbOCH$_3$ and provide initial spectroscopic characterization.

For the 2D spectroscopy [45–47] and DLIF measurements, the free-jet expansion is probed approximately 10 cm downstream from the source using radiation from an excimer-pumped, tunable, pulsed-dye laser (∼10 ns pulse width, ∼3 cm^{-1} linewidth). The molecular laser-induced fluorescence (LIF) is focused into a 0.67-m, high-efficiency (f number = 6.0) Czerny-Turner-type monochromator with a low-dispersion grating (300 lines/mm). The DLIF from the grating is imaged on a cooled and temporally gated intensified charge-coupled device (ICCD). The CCD array is binned to produce an array of intensities versus emission wavelength. The ICCD can be gated with resolution <1 ns, which enables temporal separation of the LIF from background light due to the dye laser and ablation plume. The ICCD gate width is typically set to 200 ns and delayed 10 ns after the pulsed laser. The wavelength calibration and relative sensitivity of the spectrometer were calibrated prior to data collection using an argon pen lamp and blackbody source.

High-resolution measurements are performed in a separate apparatus, as in Ref. [44]. The molecular beam is produced as described above but skimmed in order to reduce Doppler broadening. A single-frequency, cw dye laser (linewidth ∼1 MHz) is used to excite the molecules, and the resulting fluorescence is detected on a cooled photomultiplier tube (PMT). Laser powers of approximately 20 mW are used, resulting in comparable power- and Doppler-broadened linewidths, typically ∼0.001 cm^{-1}.

III. OBSERVATIONS

A. 2D spectroscopy

Initial survey scans used 2D (excitation vs DLIF) spectroscopy to search for YbOCH$_3$ fluorescence. A 75-nm-wide

TABLE I. Vibrational normal-mode numbering and symmetry labels for MOCH$_3$ molecules under transformations of the C_{3v} point group.

Mode	Symmetry	Description
ν_1	a_1	CH$_3$ symmetric stretch
ν_2	a_1	CH$_3$ symmetric bend
ν_3	a_1	O-C stretch
ν_4	a_1	M-O stretch
ν_5	e	CH$_3$ asymmetric stretch
ν_6	e	CH$_3$ asymmetric bend
ν_7	e	O-CH$_3$ wag
ν_8	e	M-O-C bend

fluorescence spectral window was monitored while scanning the excitation laser wavelength. To facilitate data analysis, this window tracked the excitation laser as it was scanned. The pulsed-dye laser was scanned over a range of about 400 cm^{-1} near the YbOH $\tilde{A}\,^2\Pi_{1/2} \leftarrow \tilde{X}\,^2\Sigma^+$ origin band (17 323 cm^{-1} [44]). A strong and broad fluorescence signal was observed at around 17 271 cm^{-1}. The 2D spectrum in the vicinity of this signal is shown in Fig. 1(a). The ground-state vibrational frequencies observed in emission closely matched those expected of YbOCH$_3$, leading to an initial assignment of this as the YbOCH$_3$ $0_0^0\,\tilde{A}\,^2E_{1/2} \leftarrow \tilde{X}\,^2A_1$ band. (For convenience, we include the vibrational normal-mode numbering and symmetry labeling in Table I.) Ytterbium monohydroxide is also produced in the ablation reaction, and by comparing the intensities of the two species's origin bands we estimate that we produced about an order of magnitude more YbOCH$_3$ than YbOH.

We obtain the excitation spectra shown in Fig. 1(b) by vertically integrating $\pm$2-nm slices of the off-resonance fluorescence. Similarly, Fig. 1(c) is obtained by vertical integration of the on-resonance fluorescence. Horizontal integration at fixed excitation wave number can be used to obtain dispersed fluorescence traces, although these have lower resolution than the DLIF measurements described in Sec. III B.

The on-resonance detected excitation spectrum [Fig. 1(c)] exhibits an intense, sharp, blue-degraded band near 17 271 cm^{-1} which is assigned as the $0_0^0\,\tilde{A}\,^2E_{1/2} \rightarrow \tilde{X}\,^2A_1$ emission. The excitation spectrum is quite compact, implying that the geometry changes little upon excitation and that the electronic orbital angular momentum in the $\tilde{A}\,^2E$ state is largely unquenched (i.e., $\zeta_e \approx 1$) [48,49]. The off-resonance excitation spectrum, shown in Fig. 1(b), is obtained by vertical integration over a $\pm$2 nm range centered $\sim$130 cm^{-1} to the red of the excitation wavelength (i.e., by monitoring the Stokes-shifted emission). The extracted excitation spectrum exhibits both the sharp band near 17 271 cm^{-1} and a weaker, broader, and unstructured fluorescence feature near 17 281 cm^{-1}. The latter is assigned as excitation from $\tilde{X}\,^2A_1(v=0)$ to a state of unknown character that we simply designate as [17.28]. The relative intensities of the bands at 17 271 cm^{-1} and 17 281 cm^{-1} for the on- and off-resonance detection suggest that the bending mode in the [17.28] state is quite active.

Also evident in the 2D spectrum are Stokes-shifted signals centered about 400 cm^{-1} and 535 cm^{-1} to the red of the excitation. These are assigned as $4_0^1\,\tilde{A}\,^2E_{1/2} \rightarrow \tilde{X}\,^2A_1$ and $4_1^0 8_1^0\,\tilde{A}\,^2E_{1/2} \rightarrow \tilde{X}\,^2A_1$, respectively (with similar assignments for the [17.28] bands). Again, the relative intensities of these bands suggest higher bending mode activity in the [17.28] state. It is noteworthy that in YbOH there is also an unassigned vibronic state approximately 10 cm^{-1} above the $\tilde{A}\,^2\Pi_{1/2}(000)$ state [24]. A key difference is that in YbOCH$_3$ this higher-energy state couples preferentially to the Yb-O-C bending mode, while in YbOH the analogous level exhibits a DLIF spectrum nearly identical to the diagonal origin band.

We also recorded 2D spectra in the vicinity of several bands involving excited vibrational levels in the $\tilde{X}\,^2A_1$ and $\tilde{A}\,^2E$ states. A weak feature was observed about 130 cm^{-1} to the red of the origin band near the expected $8_1^0\,\tilde{A}\,^2E_{1/2} \leftarrow \tilde{X}\,^2A_1$ vibronic transition. We observed two bands near the expected position of the $4_0^1\,\tilde{A}\,^2E_{1/2} \leftarrow \tilde{X}\,^2A_1$ transition, approximately 400 cm^{-1} above the origin band [Fig. 2(a)]. These bands, near 17 641 cm^{-1} (designated as the [17.64] state) and 17 681 cm^{-1} (designated as the [17.68] state), are blueshifted by 370 and
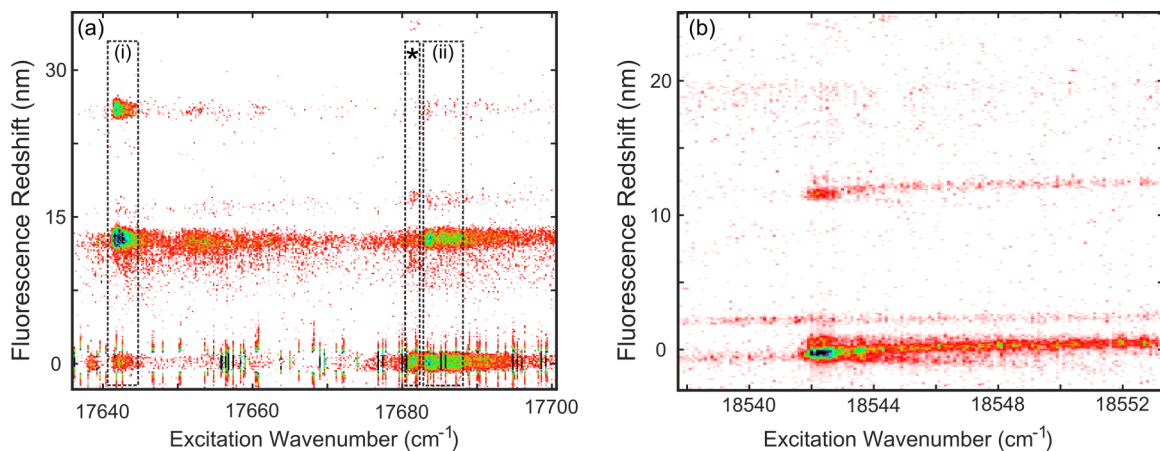

FIG. 2. (a) Pulsed-dye laser 2D spectrum in the vicinity of the $4_0^1\,\tilde{A}\,^2E_{1/2} \leftarrow \tilde{X}\,^2A_1$ bands. Integration at fixed fluorescence wavelength can be used to obtain excitation spectra. The DLIF features near 17 641 cm^{-1} (marked "(i)") and 17 683 cm^{-1} (marked "(ii)") are shown in Fig. 4. The weak feature marked by an asterisk is due to the YbOH [17.68] band. (b) Pulsed-dye laser 2D spectrum in the vicinity of the $0_0^0\,\tilde{A}\,^2E_{3/2} \leftarrow \tilde{X}\,^2A_1$ band.
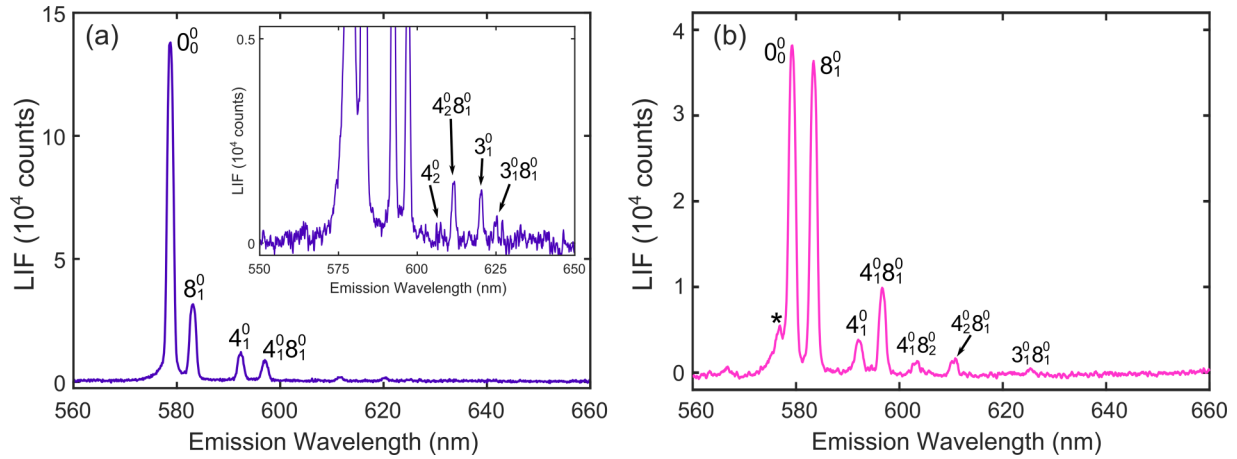
FIG. 3. DLIF spectrum resulting from excitation of the $0_0^0 \tilde{A} \, ^2E_{1/2} \leftarrow \tilde{X} \, ^2A_1$ bandhead. Numbers above each peak indicate transition assignments using the vibrational labeling of Table I. (a) YbOCH$_3$, excitation at 17 271.1 cm^{-1}. Inset: expanded vertical axis to emphasize the weakest decay features observed. (b) YbOCD$_3$, excitation at 17 249.7 cm^{-1}. The small shoulder marked by an asterisk is attributed to impurity YbOH/YbOD.

410 cm^{-1} relative to the origin band. Based on the long observed progressions in the Yb-O stretching mode, these levels both appear to have strong $v_4 = 1$ character (see Sec. III B). This observation is similar to YbF, where two closely spaced excited states (the [557] and [561] states) have substantial $v = 1$ character [43,50]. Fluorescence from these states do not show the strong activity in the v_8 mode that was observed on the origin band.

In addition, we explored a region approximately 1300 cm^{-1} above the origin band, where the $\tilde{A} \, ^2E_{3/2} \leftarrow \tilde{X} \, ^2A_1$ transition would be expected. As shown in Fig. 2(b), a band was observed near 18 540 cm^{-1} with weak off-diagonal decays at frequencies matching the YbOCH$_3$ v_4 and v_8 modes. This implies an effective spin-orbit constant of $a\zeta_e d \approx 1270$ cm^{-1}, similar to that of YbF [51] and YbOH [52], indicating that the spin-orbit interaction is not significantly quenched.

The $\tilde{A} \, ^2E_{1/2}(v = 0)$ vibronic state radiative lifetime was measured by fixing the dye laser wavelength to the $0_0^0 \tilde{A} \, ^2E_{1/2} \leftarrow \tilde{X} \, ^2A_1$ band head and recording the DLIF spectrum at variable time delay after the pulsed-laser excitation. The ICCD gate (200 ns wide) was delayed after the pulsed-dye laser in steps of $\sim$3 ns and the resulting fluorescence fit to an exponential to determine the excited state lifetime. The radiative lifetime of the $\tilde{A} \, ^2E_{1/2}(v = 0)$ level is determined to be 37(4) ns, somewhat longer than the value of 22(2) ns for the $\tilde{A} \, ^2\Pi_{1/2}(000)$ state of YbOH [24].

B. Dispersed fluorescence

Higher-resolution DLIF spectra were recorded by fixing the excitation laser wavelength and reducing the entrance slit of the monochromator. Typically 5000 ablation pulses were coadded to achieve sensitive measurement of the vibrational frequencies and branching ratios. Background traces were recorded separately to eliminate scattered light due to either the probe or ablation laser.

The DLIF spectrum resulting from pulsed-dye laser excitation at the YbOCH$_3$ band head ($\sim$17 271 cm^{-1}) is shown

in Fig. 3(a). The measured vibrational intervals are listed in Table II, and vibrational frequencies are extracted as discussed in Sec. V A. The DLIF is consistent with a relatively diagonal FCF matrix, as expected. A short progression in v_4 (the Yb-O stretching mode) is observed, with relative intensities similar to those of YbOH [24]. We observed prominent decay to v_8 (Yb-O-C bending mode), which was unexpected because the $8_1^0 \tilde{A} \, ^2E_{1/2} \rightarrow \tilde{X} \, ^2A_1$ transition is nominally forbidden by symmetry. Vibronic coupling due to the (pseudo)-Jahn-Teller interaction has previously been invoked to explain similar decays in CaOCH$_3$ [53]. We do not observe fluorescence at $2v_8$, which is symmetry allowed. Weak features associated with the v_3 (C-O stretch) are also observed, and the frequencies and branching ratios are consistent with values observed in CaOCH$_3$ [36,53].

Isotopic studies aided in the assignment of the ligand-centered vibrations. Figure 3(b) displays the DLIF spectrum following excitation in YbOCD$_3$ and vibrational frequencies extracted from these data are listed in Table II. The origin band of YbOCD$_3$ was found near 17 250 cm^{-1}. This $\approx$20-cm^{-1} isotope shift is similar to the large shift ($\approx$10 cm^{-1}) observed upon deuteration of CaOCH$_3$ [40]. Interestingly, the branching ratios observed for YbOCD$_3$ differ strikingly from those observed in YbOCH$_3$, although the frequencies agree well with the expected isotope shifts.

We have also measured DLIF spectra following excitation to bands near the expected position of the $\tilde{A} \, ^2E_{1/2}(v_4 = 1)$ state. As described above, two such states were found near 17 641 and 17 683 cm^{-1}, which we call the [17.64] and [17.68] states, respectively. DLIF measurements from these levels are shown in Figs. 4(a) and 4(b). These spectra both show strong decays to a progression in v_4, confirming the large $v_4 = 1$ character of each excited state. Weak features associated with decay to $v_8 = 1$ are also observed, although with significantly lower intensity than observed on the origin band. The presence of two states with significant $v_4 = 1$ character is likely due to mixing of the $\tilde{A} \, ^2E_{1/2}(v_4 = 1)$ vibronic level with vibronic levels of states associated with f-orbital vacancies, e.g., ([Xe]$4f^{13}6s^2$)$_{\text{Yb}^+}$, similar to the case of YbF

TABLE II. Observed and calculated (*ab initio*) vibrational intervals in $\tilde{X}\ ^2A_1$ for YbOCH$_3$ and YbOCD$_3$. Calculated values are in the harmonic approximation. Previously measured values for alkaline-earth monomethoxides are included for comparison. All frequencies are in cm^{-1}. Typical measurement error bars are ± 5 cm^{-1} depending upon signal-to-noise ratio and proximity to argon emission calibration lines.

Mode	YbOCH$_3$ (meas.)	YbOCH$_3$ (calc.)	YbOCD$_3$ (meas.)	YbOCD$_3$ (calc.)	SrOCH$_3$[a]	CaOCH$_3$[b]
ν_3	1151	1154		1085	1138	1156
ν_4	400	390	370	369	405	487
ν_8	130	134	120	124	135	142
$2\nu_8$	260	268		248		-
$\nu_4 + \nu_8$	533	524	500	493		625
$2\nu_4$	805	780		738	806	973
$2\nu_4 + \nu_8$	933	914	880	862		-
$\nu_4 + 2\nu_8$	-	658	680	617		-
$\nu_3 + \nu_8$	1287	1288	1270	1262		-
$3\nu_4$	1197	1170				-
$4\nu_4$	1576	1560				-
$5\nu_4$	1972	1950				-

[a]Measured values from Refs. [34] and [37].
[b]Measured values from Ref. [37].

[43,50]. It is noteworthy that the LIF excitation spectrum of YbOH [24], which is present as an impurity in our sample, also exhibits two relatively weak features at 17 643 and 17 681 cm^{-1}. Fortunately, the associated YbOH DLIF spectra are readily distinguishable from those resulting from emission of the [17.64] and [17.68] states of YbOCH$_3$.

C. cw excitation and DLIF spectra

The high-resolution spectrum recorded near the $0_0^0\ \tilde{A}\ ^2E_{1/2} \leftarrow \tilde{X}\ ^2A_1$ band head identified above is shown in Fig. 5(a). The spectrum is quite congested due to the presence of several isotopes of Yb with relatively high natural abundance, including ^{174}Yb (32%), ^{172}Yb (22%), ^{173}Yb (16%), ^{171}Yb (14%), and ^{176}Yb (13%). A full analysis of the high-resolution spectra will be the focus of a future publication, where lower rotational temperature and isotope-selective enhanced production [39,54] is used to greatly reduce the complexity of the spectrum. We make some qualitative observations here, showing the spectrum is consistent with a $^2E_{1/2} \leftarrow\ ^2A_1$ transition.

The rotational energy-level structure of a $^2A_1$ state is that of an open-shell prolate symmetric top molecule near the Hund's case (b) limit. For an MOCH$_3$ species, the $K_R'' = 1$ stack of levels begins approximately 6 cm^{-1} ($\approx A''$) above the $K_R'' = 0$ stack. The $|K_R''| = 1$ levels obey different nuclear spin statistics and will also be populated significantly and show prominently in the spectrum. The energy-level pattern of a $^2E_{1/2}$ state is that of an open-shell prolate symmetric top near the Hund's case (a) limit. The parity doubling in the $K_R' = 0, K' = 1$ level is expected to be large, and hence the dominant $\tilde{A}\ ^2E_{1/2}(K_R' = 0, K' = 1) \leftarrow \tilde{X}\ ^2A_1(K_R'' = 0)$ band is expected to have the same general appearance as the $\tilde{A}\ ^2\Pi_{1/2} \leftarrow \tilde{X}\ ^2\Sigma^+$ band of YbOH. Indeed, we observe that the high-resolution spectrum is reminiscent of the $\tilde{A}\ ^2\Pi_{1/2} \leftarrow \tilde{X}\ ^2\Sigma^+$ origin band of YbOH due to the sharply peaked, blue-degraded band head and the widely spaced peaks in the P/R branches [24,44]. Using the expected YbOCH$_3$ rotational constant B, determined by either empirically scaling parameters for YbOH or by *ab initio* calculations, we estimate that these peaks are spaced by approximately $4B$. This branch spacing
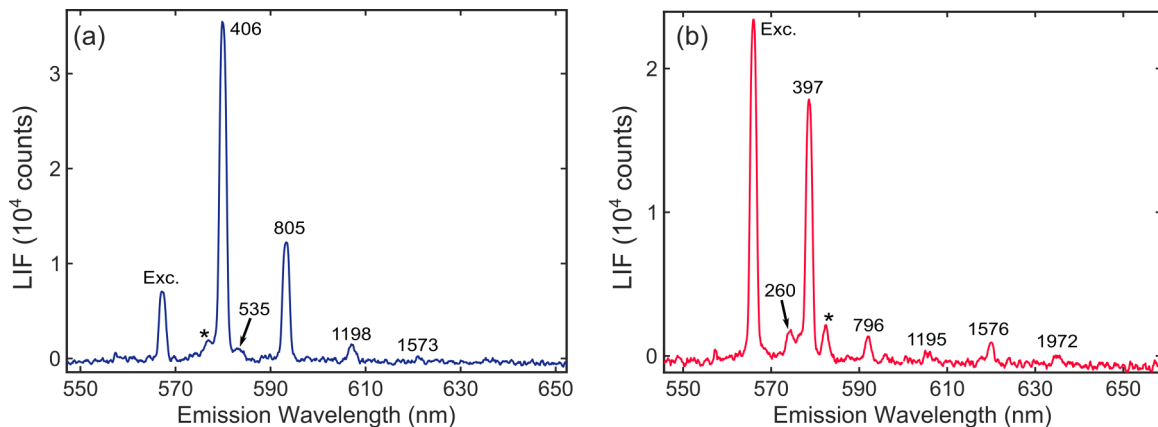

FIG. 4. DLIF spectrum resulting from excitation at (a) 17 641.75 cm^{-1} and (b) 17 683.40 cm^{-1}. The numbers above the spectral features are the measured shifts (in cm^{-1}) relative to the excitation wavelength ("Exc."). Features marked by an asterisk are due to YbOH impurity fluorescence, as described in the text.
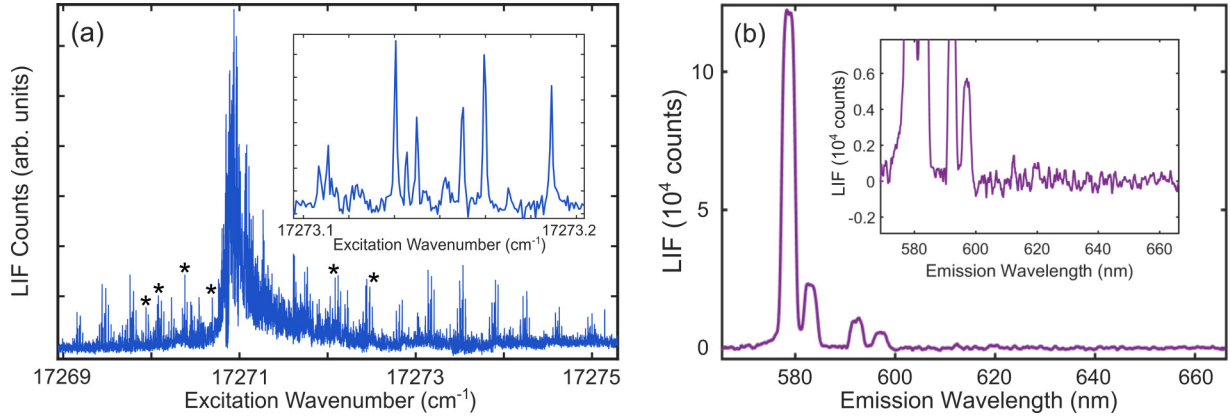
FIG. 5. (a) High-resolution excitation spectrum near the YbOCH$_3$ 0^0_0 $\tilde{A}$ $^2E_{1/2} \leftarrow \tilde{X}$ $^2A_1$ bandhead. Features marked by an asterisk were selected for cw-excitation DLIF measurements. Inset: Details of spectrum near 17 273.15 cm^{-1}, with isotopic and K-stack structure visible. (b) DLIF spectrum resulting from rotationally resolved, cw-dye laser excitation at 17 270.970 cm^{-1}. Inset: Zoom near signal baseline to show the relative intensity sensitivity of the measurement.

implies an excited-state parity doubling $\epsilon_1 - 2h_1 \approx B$ [55].[2] Here, $\epsilon_1 - 2h_1$ plays the role of the usual $p + 2q$ (Λ-type doubling) parameter in a linear $^2\Pi$ state [56]. Note that a similar branch spacing of about $4B$ is observed in the YbOH $\tilde{A}$ $^2\Pi_{1/2} \leftarrow \tilde{X}$ $^2\Sigma^+$ origin band [44].

We recorded several DLIF spectra using single-frequency, cw-dye laser excitation on selected rotational lines. These measurements were used to eliminate the possibility that the strong symmetry-forbidden decays observed above originate from the pulsed laser simultaneously exciting many quantum states and/or isotopologues. We selected a few rotationally resolved transitions for cw-excitation DLIF spectra. The selected transitions, marked by asterisks in Fig. 5(a), were chosen based on their relative isolation and preliminary assignment of $K' = 0$ and $K' = 1$ character. A representative cw-excitation DLIF spectrum is shown in Fig. 5(b). The sensitivity of the cw-dye laser measurements is lower than that of the pulsed-dye laser measurements due to decreased signal and an inability to temporally exclude the excitation light. This loss in sensitivity required enlarging the entrance slit on the monochromator, lowering the spatial resolution. DLIF spectra recorded on other rotationally resolved transitions yielded VBRs consistent with those of Fig. 5(b) and with the pulsed-laser excitation spectra. These measurements confirmed that the VBRs determined from the pulsed-dye laser excitation are not strongly dependent on the rotational state selected.

IV. ANALYSIS

A. Vibrational structure

The wavelength axes of the DLIF spectra were calibrated and linearized prior to data collection. Ground-state vibrational intervals were determined from the DLIF spectra

by locally fitting each peak and taking appropriate differences. The measured frequencies and assignments are listed in Table II along with comparisons to the alkaline-earth monomethoxides SrOCH$_3$ and CaOCH$_3$. The observed ground-state vibrational energies were fit to the phenomenological expression [57]

$$E(v) = \sum_i \omega_i \left(v_i + \frac{d_i}{2} \right) + \sum_{i,k} x_{ik} \left(v_i + \frac{d_i}{2} \right)^2, \quad (1)$$

where mode i has degeneracy d_i, frequency ω_i, and v_i quanta of excitation. The constants x_{ik} denote the leading anharmonic corrections. Only the observed modes (ν_3, ν_4, and ν_8) were included in the fit. The fit incorporated DLIF traces with pulsed-dye laser excitation to the $\tilde{A}(v = 0)$, [17.64], and [17.68] states. The results of this fit are presented in Sec. V A.

B. Vibrational branching ratios

Vibrational branching ratios (VBRs), $b_{v',v''}$, were determined by the ratios of integrated areas under each observed peak. These are related to the FCFs by [58]

$$b_{v',v''} = \frac{I_{iv',fv''}}{\sum_{fv''} I_{iv',fv''}}$$

$$\approx \frac{\text{FCF}_{iv',fv''} \times \nu^3_{iv',fv''}}{\sum_{fv''} \text{FCF}_{iv',fv''} \times \nu^3_{iv',fv''}}, \quad (2)$$

where i and f label initial and final states, respectively. Table III lists the observed vibrational branching ratios and FCFs determined for the YbOCH$_3$ $\tilde{A}$ $^2E_{1/2} - \tilde{X}$ $^2A_1$, [17.64] $- \tilde{X}$ $^2A_1$, and [17.68] $- \tilde{X}$ $^2A_1$ bands. The spectrometer and ICCD relative intensity sensitivities were calibrated prior to data collected. The typical noise level of the DLIF spectra corresponds to $\sim$100 counts per pixel, equivalent to $\sim$1 part in 10^3 relative to the dominant peak. Systematic errors associated with the calibration lead to $\sim$5% relative

---

[2]In this expression, ϵ_1 is a higher-order spin-rotation parameter and h_1 is a Jahn-Teller parameter [40].

TABLE III. Branching ratios and FCFs from the $\tilde{A}\ ^2E_{1/2}(v=0)$, [17.64], and [17.68] states of YbOCH$_3$ to the $\tilde{X}\ ^2A_1$ levels. Values are determined from the pulsed-dye laser excitation DLIF spectra. After accounting for the detection noise and systematic uncertainties due to calibration, the noise levels of the smallest VBRs are $\pm 0.7 \times 10^{-3}$ for the 0^0_0 band and $\pm 2 \times 10^{-3}$ for the [17.64] and [17.68] bands.

| | $\tilde{A}\ ^2E_{1/2}(v=0)$ | | [17.64] | | [17.68] | |
	VBR	FCF	VBR	FCF	VBR	FCF
0_0	0.729	0.7184	0.132	0.122	0.526	0.504
8_1	0.164	0.1653				
4_1	0.054	0.0566	0.624	0.617	0.375	0.385
$4_1 8_1$	0.038	0.0413	0.0181	0.0183	0.044	0.046
4_2	9.89×10^{-4}	1.1×10^{-3}	0.201	0.214	0.0268	0.0293
$4_2 8_1$	6.8×10^{-3}	7.9×10^{-3}				
3_1	5.49×10^{-3}	6.7×10^{-3}				
$3_1 8_1$	2.13×10^{-3}	2.65×10^{-3}				
4_3			0.021	0.0244	5.13×10^{-3}	6.02×10^{-3}
4_4			3.6×10^{-3}	4.36×10^{-3}	0.015	0.0194
4_5					7.6×10^{-3}	1.0×10^{-2}

uncertainty in peak height near 580 nm and $\sim$10% relative uncertainty near 630 nm.

C. Electronic structure calculations

To aid assignment of the DLIF spectra, *ab initio* calculations were performed for YbOCH$_3$ and YbOCD$_3$ using the ORCA quantum chemistry program [59,60]. Molecular orbitals, optimized geometries, normal modes, and vibrational frequencies for the ground electronic state were calculated at the level of unrestricted Kohn-Sham (UKS) density-functional theory (DFT) using the B3LYP functional [61,62]. We carefully studied the accuracy of various basis-set and functional choices. Final calculations employed a quadruple-ζ basis set, including two sets of polarization functions and diffuse orbitals on the heavy atoms. A 28-electron small-core pseudopotential was used for the Yb atom [63–65]. Time-dependent DFT (TD-DFT) was used to model the $\tilde{A}\ ^2E$ state, using the same basis and functional as were used for the ground electronic state. This allowed computation of excitation energies and geometry optimization using analytic Hessians. Vibrational frequencies were determined via numerical differentiation. The theoretical methods were validated by performing test calculations for YbOH and CaOCH$_3$. See Appendix for comparison between different basis sets, validation against previous measurements, and additional computational outputs.

V. DISCUSSION

The primary purpose of this investigation was to observe YbOCH$_3$ and determine its suitability for laser cooling and precision tests of fundamental physics. The short radiative lifetime and reasonably diagonal FCFs indicate that YbOCH$_3$ is a promising candidate for these applications, similar to YbF [43,66,67] and YbOH [22]. The data provide information necessary to begin further studies of optical cycling and vibrational repumping. As discussed below, YbOCH$_3$ also presents an interesting platform for future studies of (pseudo-)Jahn-Teller interaction in the presence of strong spin-orbit coupling.

A. The $\tilde{X}\ ^2A_1$ state

Assignments of the observed vibrational decays were relatively straightforward using the *ab initio* predictions, isotopic data, and comparison to alkaline-earth monomethoxides. For the origin band, the peaks redshifted by 130 and 400 cm^{-1} are assigned to 8^0_1 and 4^0_1, respectively. The feature redshifted by 1150 cm^{-1} is near the expected frequency of either ν_3 (1× O-C stretch) or $3\nu_4$ (3× Yb-O stretch). Because this decay has a stronger intensity than 4^0_2, we favor the assignment to 3^0_1. Furthermore, the DLIF spectra from the [17.64] and [17.68] states show a feature at slightly higher frequency ($\approx$1170 cm^{-1}) that is assigned to $3\nu_4$. The weak feature redshifted by $\sim$1280 cm^{-1} is assigned to the decay $3^0_1 8^0_1$ based on the predicted frequencies for various combination bands. In addition, the relative intensity of this feature to the 3^0_1 peak is roughly consistent with the strengths of other combination bands involving ν_8.

The vibrational frequencies are determined by fitting observed vibrational energy intervals to Eq. (1). We find $\omega_3 = 1152(5)$ cm^{-1}, $\omega_4 = 405(3)$ cm^{-1}, $\omega_8 = 130(3)$ cm^{-1}, and $x_{44} = -2.0(6)$ cm^{-1}. These fitted frequencies agree well with the computed harmonic frequencies and with the corresponding values for CaOCH$_3$ and SrOCH$_3$ after accounting for differences in reduced mass [37]. The anharmonic contribution to the Yb-O stretching mode is similar to that observed in YbOH in both magnitude and sign [24]. Finally, the fitted value ω_3 is similar to that predicted for the methoxy anion, consistent with a highly ionic metal-ligand bond [68].

Our *ab initio* calculations predict that the $\tilde{X}\ ^2A_1$ state has a linear Yb-O-C bond and symmetric, off-axis H atoms with C_{3v} symmetry, just like the alkaline-earth monomethoxides. The calculated values $r_{OC} = 1.39$ Å and $r_{CH} = 1.10$ Å for YbOCH$_3$ are quite similar to those measured in CaOCH$_3$ ($r_{OC} = 1.411(7)$ Å and $r_{CH} = 1.094$ Å) [40], while the calculated value of $r_{YbO} = 2.04$ Å for YbOCH$_3$ is very close to the measured value for YbOH ($r_{YbO} = 2.0397$ Å) [22]. In addition, our *ab initio* calculations predict a molecule-frame dipole moment of $\mu(\tilde{X}) = 2.2$ D in the $\tilde{X}\ ^2A_1$ ground state. This is nearly identical to the ground-state dipole moment of

YbOH [1.9(2) D [44]] and comparable to that of CaOCH$_3$ [1.58(8) D [35]]. These calculations also report the $\tilde{X}$ $^2A_1$ electronic state arises primarily from Yb-centered $6s\sigma$ (65%) and $6p\sigma$ (15%) orbitals. This is quite similar to YbF, where experimental analysis of the hyperfine structure showed that the X $^2\Sigma^+$ state had 57% $6s$ character [69]. The resulting polarization of the valence electron away from the Yb-O bond is consistent with the predicted molecule-frame dipole moment being significantly smaller than that of an electrostatic model with point charges located near the Yb$^+$ and OCH$_3^-$ moieties [49]. Together, these results help confirm the expectation that YbOCH$_3$ in the $\tilde{X}$ $^2A_1$ ground state conforms to many of the patterns established by previous studies of alkaline-earth monomethoxides. The predicted vibrational frequencies for YbOCH$_3$ and YbOCD$_3$ show excellent agreement with our measurements, as can be seen in Table II. Although we only observed activity in three of the vibrational modes, we report the full results of the vibrational structure in Appendix.

B. The excited states

We have observed a number of excited states assigned to YbOCH$_3$, associated with bands near 17 271 cm^{-1}, 17 281 cm^{-1}, 17 641 cm^{-1}, 17 683 cm^{-1}, and 18 542 cm^{-1}. The band at 17 271 cm^{-1} is assigned to terminate on the $\tilde{A}$ $^2E_{1/2}(v = 0)$ level. As discussed above, both the [17.64] and [17.68] states seem to have strong $v_4 = 1$ (Yb-O stretching) character, but on the basis of the FCF measurements we tentatively assign the [17.64] state as dominantly $\tilde{A}$ $^2E_{1/2}(v_4 = 1)$, while the [17.68] state appears to be a perturbing state similar to those observed in both YbF [43] and YbOH [24]. The band near 18 542 cm^{-1} is tentatively assigned as $0_0^0\tilde{A}$ $^2E_{3/2} \leftarrow \tilde{X}$ $^2A_1$. This implies an effective spin-orbit splitting $a\zeta_e d \approx$ 1270 cm^{-1}, similar to that of YbF [51] and YbOH [52]. Future high-resolution studies will be useful to provide further confirmation of these assignments.

Observation of the relatively intense 8_1^0 feature in the $\tilde{A}$ $^2E_{1/2}(v = 0)$ DLIF spectrum (Fig. 3) was at first unexpected because, assuming both the $\tilde{X}$ and $\tilde{A}$ states have C_{3v} symmetry, the ν_8 mode is of e symmetry, and this decay is symmetry forbidden within the Born-Oppenheimer (BO) approximation. One possible explanation for the strength of this transition is that YbOCH$_3$ possesses a bent geometry (C_s symmetry) in the $\tilde{A}$ state. We disfavor this explanation for several reasons. First, we do *not* observe emission from $\tilde{A}$ $^2E_{1/2}$ to $\tilde{X}$ $^2A_1(v_8 = 2)$, which would be expected if there were significant geometrical change upon electronic excitation. Similarly, we do not observe strong decays to $\tilde{X}$ $^2A_1(v_8 = 1)$ from the [17.64] or [17.68] states. Second, a bent excited state would likely be accompanied by significant quenching of the electronic orbital angular momentum, but the above assignment of the $\tilde{A}$ $^2E_{3/2}$ state is consistent with $a\zeta_e d \approx$ 1270 cm^{-1}, indicating little quenching. Third, we did not observe rotational bands associated with the K_a structure expected for a bent molecule; the contour of the high-resolution spectra could be well simulated using a symmetric top Hamiltonian. A more detailed discussion of the high-resolution spectrum will be the subject of a separate publication.

Instead, we attribute the relatively strong 8_1^0 signal to spin-orbit vibronic coupling. Following Ref. [36], we consider the possibility of Jahn-Teller coupling within $\tilde{A}$ ^2E, characterized by parameter k_8, and pseudo-Jahn-Teller coupling between $\tilde{A}$ ^2E and nearby states of A_1 symmetry, characterized by parameter λ_8. Here we assume that ν_8 is the only mode with significant Jahn-Teller activity. Spin-orbit coupling between $\tilde{A}$ ^2E and $\tilde{B}$ $^2A_1$ can interfere with (pseudo-)Jahn-Teller terms and lead to a second-order, effective coupling between the $\tilde{A}$ $^2E(v_8 = 1)$ and $\tilde{A}$ $^2E(v_8 = 0)$ vibronic levels. Given the intensity of the 8_1^0 feature, we infer an effective matrix element

$$\langle \tilde{A}\ ^2E_{1/2}, v_8 = 1 | H_{JT} | \tilde{A}\ ^2E_{1/2}, v_8 = 0 \rangle \approx 50\,\text{cm}^{-1}.$$

Again, following Ref. [36], we may also express this matrix element as $k_8 + 2C_{AB}\lambda_8$. The first term represents direct coupling between $\tilde{A}$ $^2E(v_8 = 0, 1)$ while the second term represents the spin-orbit vibronic coupling via an intermediate $^2A_1$ state. C_{AB} is the mixing induced by spin-orbit coupling between $\tilde{A}$ ^2E and $\tilde{B}$ $^2A_1$, approximated using the measured spin-orbit parameter of YbOCH$_3$ and the estimated $\tilde{B}$ $^2A_1$ energy scaled from YbF. It has been shown for CaOCH$_3$ that the k_8 term is negligible compared to the λ_8 term. Assuming the same holds for YbOCH$_3$, we estimate $\lambda_8 \approx 55$ cm^{-1}. This is approximately three times smaller than the value of λ_8 computed by *ab initio* methods for CaOCH$_3$, which is consistent with the expected trend as spin-orbit coupling strength increases [70]. Though preliminary, this estimate shows that the strong 8_1^0 feature can be explained reasonably by the spin-orbit vibronic coupling mechanism.

Recent studies of CaOCH$_3$ by our group lend support to these quantitative estimates. In those measurements, which will be discussed in more detail elsewhere, we observed the analogous vibronically induced 8_1^0 feature in CaOCH$_3$, albeit with weaker VBR $\approx 3 \times 10^{-3}$. Note that this agrees quite well with the *ab initio* prediction of Ref. [36], where the decay was predicted but not observed. Applying the same analysis as used above, we determine a linear pseudo-Jahn-Teller coefficient for CaOCH$_3$ of $\lambda_8^{\text{CaOCH}_3} \approx 145$ cm^{-1}. This is in good agreement with the *ab initio* value of 150 cm^{-1} [36] and provides a satisfactory check of the estimation methods used above. Nonetheless, *ab initio* treatment of the vibronic coupling problem in YbOCH$_3$ would be highly desirable. In addition, we note that other interpretations are possibly valid, such as the k_8 parameter being non-negligible or vibronic coupling between $\tilde{A}$ ^2E and nearby electronic states arising from excitations of Yb $4f$ electrons. The presence of a strong perturbation makes it very challenging to use standard semiempirical methods [24,41,53] to predict the FCFs in YbOCH$_3$. This reinforces the need for careful experimental studies to guide future experiments with this molecule.

TD-DFT calculations targeting the $\tilde{A}$ ^2E state predict an excitation energy $T_e = 18\,060$ cm^{-1}. This is in good agreement with the measured value of $T_e \approx 17\,900$ cm^{-1} (accounting for the spin-orbit coupling). The $\tilde{A}$ ^2E state is predicted to have C_{3v} symmetry, with bond lengths/angles $r_{\text{YbO}} = 2.010$ Å, $r_{\text{OC}} = 1.396$ Å, $r_{\text{CH}} = 1.095$ Å, and $\theta_{\text{OCH}} = 111.283°$. The calculations predict a linear Yb-O-C structure. The predicted change in Yb-O bond length is quite similar to that observed for YbOH and consistent with the relatively

diagonal branching ratios [44]. The calculation predicts a vibrational frequency $\omega_4 = 410$ cm^{-1}, which is in reasonable agreement with the splitting observed between the $\tilde{A}\ ^2E$ and [17.64]/[17.68] states. See Appendix for a full set of predicted excited-state vibrational frequencies.

C. Prospects for laser cooling and trapping

Our measurements confirm the viability of achieving rapid photon cycling with YbOCH$_3$. The short radiative lifetime of the $\tilde{A}$ state (corresponding to $\Gamma \approx 27 \times 10^6$ s^{-1}) will enable large optical forces, comparable to those of previously laser-cooled molecules. Based on our VBR measurements, a feasible laser-cooling scheme requiring about eight distinct laser wavelengths will achieve vibrational closure below a part in 10^3. Additional frequencies required for repumping the rotational and spin-rotation substructure can be added as laser frequency sidebands using electro- or acousto-optic modulators. Assuming a cryogenic buffer-gas beam containing 10^9 YbOCH$_3$ molecules and a loss probability per photon scatter of $< 1 \times 10^{-3}$ (the smallest observed VBR) to unaddressed vibrational states, this scheme would leave $\sim 10^4 - 10^5$ YbOCH$_3$ molecules in a "bright" state following $\sim 10\,000$ photon scatters. This is comparable to the experimental complexity required to laser cool much lighter (and simpler) species [30,53,71]. Laser-enhanced molecule production such as that demonstrated for YbOH [54] could increase the molecule number by at least an order of magnitude. The presence of multiple excited electronic states with strong electric-dipole allowed transitions to excited vibrational states in $\tilde{X}$ provides a convenient method of decoupling the repumping pathways, similar to the scheme used for YbF [16].

D. Suitability for precision measurements

To the best of our knowledge, YbOCH$_3$ is the highest-Z symmetric top molecule amenable to optical cycling to be experimentally characterized. It is a promising system for precision tests of parity and/or time-reversal symmetry violation. In addition to the high-Z nucleus that leads to a valence electron experiencing strong relativistic effects, the presence of easily polarized, internal comagnetometer states in the $|K''| \neq 0$ manifolds allow full access to a large internal effective electric field and rejection of potential systematic errors [9,18]. Consider, for example, laser-cooled and trapped YbOCH$_3$ used for future tests of the eEDM. Under the reasonable assumptions that the internal effective electric field of YbOCH$_3$ matches that of YbOH ($\mathcal{E}_{\text{eff}} \approx 25$ GV/cm) [20,21,72] and that achievable experimental lifetimes approach 10–100 s [73–75], 10^5 trapped YbOCH$_3$ molecules and one week of averaging could provide a statistical sensitivity to the eEDM four orders of magnitude beyond the current limit [12]. This is about an order of magnitude more sensitive than an equivalent measurement in YbOH.

Even with a much smaller photon budget, transverse laser cooling and high-fidelity readout enabled by rapid photon cycling could lead to updated limits on precision tests of CP violation [76]. Consider an experiment using ^{173}YbOCH$_3$ in a molecular beam to search for a nMQM. Combining

the demonstrated production of YbOCH$_3$, enhanced chemical production [54], and transverse laser cooling using < 150 photons [30], bright beams with $> 10^7$ molecules per pulse in the science state appear possible. Forward velocities around 50 m/s and laser cooling to < 1 mK in the transverse direction [17,30] would make coherence times on the order of 10 ms feasible. Under these conditions, a sensitivity on the order of 10 μHz would be achievable with one week of averaging. Assuming (reasonably) that the nMQM sensitivity parameter is similar to that of YbOH, this would be near or below the level required to set updated limits on T-violating BSM physics, e.g., the QCD $\bar{\theta}$ parameter or the difference of quark chromo-EDMs [14,15]. Note that symmetric top molecules offer some intrinsic advantages over linear species for such measurements, such as requiring smaller laboratory electric fields for full polarization and that nuclear spin statistics ease the task of state preparation by naturally populating the $|K''| = 1$ science state [18,77].

YbOCH$_3$ is also an interesting candidate for possible tests of P violation. Recently, the degenerate bending modes in open-shell linear triatomic molecules have been proposed for tests of nuclear-spin-dependent parity violation [78,79]. Similar searches could be conducted in symmetric top molecules that meet certain structural conditions. One key requirement of such an experiment is that the ground-state parity doubling is not smaller than all spin-rotation or hyperfine structures, such that opposite-parity states with the same total angular momentum may be Zeeman-tuned into near resonance. In ^{171}YbOCH$_3$, we expect that hyperfine and K-doublet splittings will be of the same order of magnitude, ~ 0.3 MHz [35]. The size of the K doubling increases with N, so that by working in, e.g., the $N'' = 2$ or 3 state it may be possible to tune the parity doubling to be larger than the hyperfine structure. Future measurements with hyperfine resolution will be required to determine the exact splittings. Alternatively, chiral variants such as YbOCHDT may be useful for studies of parity violation arising from P-odd cosmic fields, e.g., in searches for axionlike particles [80,81]. Chiral species are predicted to be particularly sensitive to oscillating pseudovector fields that cannot be easily probed in existing spin-precession experiments [80]. Because such effects scale rapidly with Z [81], YbOCHDT may provide orders-of-magnitude increased sensitivity over previously considered chiral probes. Production and characterization of chiral ytterbium monomethyl, YbCHDT, may be especially promising by bringing the heavy nucleus closer to the chiral center.

VI. CONCLUSION

We have observed ytterbium monomethoxide, YbOCH$_3$, and performed initial measurements to assess its feasibility for laser cooling and precision measurements of CP-violating electromagnetic moments. The measured vibrational frequencies, vibrational branching ratios, and radiative lifetimes are compatible with a direct laser-cooling experiment. Electronic structure calculations have aided the vibrational assignments. We have interpreted some of the vibrational branching ratios using a simple linear vibronic coupling model. Despite having stronger off-diagonal decays than the isoelectronic species YbF and YbOH, the vibrational branching ratios in YbOCH$_3$

converge rapidly enough to permit efficient laser cooling. Even in the absence of full 3D laser cooling, YbOCH$_3$ would allow optical cycling of $\sim$150 photons with about three vibrational repumping lasers. This scale enables efficient state preparation, transverse cooling, and/or unit-efficiency readout for precision measurements in a molecular beam.

Further data are needed to sharpen the developing picture of the $\tilde{A}\,^2E_{1/2} - \tilde{X}\,^2\Pi$ band. The $\tilde{A}\,^2\Pi$ states in YbF and YbOH are quite complex due to a series of perturbing states nearby in energy [24,43], and it appears that analogous states exist in YbOCH$_3$. Careful studies of the $\tilde{A}$ state and nearby perturbing levels will be necessary to develop a laser-cooling scheme capable of scattering $\gg 10^3$ photons with YbOCH$_3$. Detailed understanding of vibronic interactions will also inform the feasibility of laser cooling increasingly complex polyatomic molecules [82]. Finally, vibronic interactions with matrix elements off-diagonal in K may lead to leakage from the optical cycle at rates high enough to require repumping. Characterizing these effects using high-resolution spectroscopy will also be important prior to laser cooling YbOCH$_3$.

APPENDIX: ADDITIONAL INFORMATION ON *AB INITIO* CALCULATIONS

Here we provide additional data to support our electronic structure calculations. Our *ab initio* calculations were performed using the ORCA quantum chemistry package [59]. Ground-state vibrational frequencies and transition dipole moments were computed using analytic B3LYP Hessians [61,62]. The excited state was modeled using time-dependent density functional theory (TD-DFT) using the same functional. The excited-state vibrational structure was computed by numerical differentiation. Initial studies used the def2-TZVPP basis set, while final calculations employed a ma-def2-QZVPP basis set [83]. A 28-electron small-core pseudopotential was used for the Yb atom [63–65]. The addition of diffuse functions to the basis set improved agreement between theory and experiment for both dipole moment and vibrational frequencies. A comparison between these choices of basis sets can be found in Tables IV and V. To validate our theoretical methods, we performed additional calculations for previously observed, relevant species. Here we report the comparison of these test calculations with experimental data. We also show the effect of basis-set quality on the computed values.

TABLE IV. Calculated properties of YbOH $\tilde{X}\,^2\Sigma^+$ state and comparison to measured values using different basis sets.

Parameter	Calc. 1[a]	Calc. 2[b]	Meas. [22,24,44]
Vibrational frequencies [cm^{-1}]			
$\nu_1(\tilde{X})$	538	530	529.33(2)
$\nu_2(\tilde{X})$	335	332	329(14)
$\nu_3(\tilde{X})$	3940	3937	
$\nu_1(\tilde{A})$		560	584[c]
$\nu_2(\tilde{A})$		329	320[d]
$\nu_3(\tilde{A})$		3950	
Bond lengths [Å]			
$r_{\mathrm{YbO}}(\tilde{X})$	2.0386	2.0441	2.0397
$r_{\mathrm{OH}}(\tilde{X})$	0.9540	0.9530	0.9270[e]
$r_{\mathrm{YbO}}(\tilde{A})$		2.012	2.006
$r_{\mathrm{OH}}(\tilde{A})$		0.9533	0.9270[f]
Dipole moment [D]			
$\mu_e(\tilde{X})$	1.6	1.8	1.9(2)
Excitation energy [cm^{-1}]			
T_e		18189	17998

[a]Using def2-TZVPP basis.
[b]Using ma-def2-QZVPP basis.
[c]Taken as the $\tilde{A}(100) - \tilde{A}(000)$ separation from Ref. [44].
[d]Taken as the $[17.64] - \tilde{A}(000)$ separation from Ref. [44].
[e]Fixed to value for BaOH, as in Ref. [22].
[f]Fixed to value for BaOH, as in Ref. [22].

Table IV reports several predictions for the $\tilde{X}\,^2\Sigma^+$ and $\tilde{A}\,^2\Pi$ electronic states of YbOH, including vibrational frequencies, geometry, and molecule-frame electric dipole moment. For the ground-state properties, we find excellent agreement between theory and experiment. We show the predicted vibrational frequencies, bond lengths, and excitation energy of the excited state. The agreement is satisfactory for the excited-state properties, with errors similar to those

TABLE V. Calculated properties of CaOCH$_3$ $\tilde{X}\,^2A_1$ state and comparison to measured values using different basis sets.

Parameter	Calc. 1[a]	Calc. 2[b]	Measured [40,53]
Vibrational frequencies [cm^{-1}]			
$\nu_3(\tilde{X})$	1140	1159	1156(5)
$\nu_4(\tilde{X})$	488	489	488(5)
$\nu_8(\tilde{X})$	139	141	144(5)
$\nu_3(\tilde{A})$		1140	1140(5)
$\nu_4(\tilde{A})$		470	501.48
$\nu_8(\tilde{A})$		150	145(5)
Bond lengths [Å] and angles [°]			
$r_{\mathrm{CaO}}(\tilde{X})$	1.958	1.969	1.962(4)
$r_{\mathrm{OC}}(\tilde{X})$	1.400	1.392	1.411(7)
$r_{\mathrm{CH}}(\tilde{X})$	1.105	1.097	1.0937
$\theta_{\mathrm{OCH}}(\tilde{X})$	111.5	111.5	111.3(2)
Dipole moment [D]			
$\mu_e(\tilde{X})$	1.1	1.4	1.58(8)
Excitation energy [cm^{-1}]			
T_e		16088	15925

[a]Using def2-TZVPP basis.
[b]Using ma-def2-QZVPP basis.

TABLE VI. Calculated vibrational frequencies for YbOCH$_3$, computed at the optimized geometry, including modes not observed in the LIF spectra presented in this manuscript. See Table I for the mode labeling and symmetry characteristics.

Vibrational mode	$\tilde{X}\ ^2A_1$ (cm^{-1})	$\tilde{A}\ ^2E$ (cm^{-1})
ν_1	2940	2961
ν_2	1482	1523
ν_3	1157	1156
ν_4	390	413
ν_5	2975	3007
ν_6	1495	1489
ν_7	1180	1181
ν_8	135	139

observed in *ab initio* calculations for related species [36,58]. The agreement in these cases supports the choice of method, especially with regard to modeling the heavy Yb atom.

Table V reports predictions for vibrational frequencies, geometry, and molecule-frame dipole moment of the $\tilde{X}\ ^2A_1$ electronic state of CaOCH$_3$. Again, we observe excellent agreement with experimental measurements. These calculations help to validate the accuracy of our computational methods for related alkaline-earth monomethoxide species.

In the experiment, only three of the eight vibrational modes were observed. Table VI reports all of the predicted vibrational frequencies for YbOCH$_3$, obtained using the quadruple-ζ basis set described above. We also include the predicted vibrational frequencies of the $\tilde{A}\ ^2E$ state of YbOCH$_3$.

[1] W. Bernreuther and M. Suzuki, The electric dipole moment of the electron, Rev. Mod. Phys. **63**, 313 (1991).

[2] M. Pospelov and A. Ritz, Electric dipole moments as probes of new physics, Ann. Phys. **318**, 119 (2005).

[3] J. Engel, M. J. Ramsey-Musolf, and U. van Kolck, Electric dipole moments of nucleons, nuclei, and atoms: The standard model and beyond, Prog. Part. Nucl. Phys. **71**, 21 (2013).

[4] D. DeMille, Diatomic molecules, a window onto fundamental physics, Phys. Today **68**(12), 34 (2015).

[5] Y. Nakai and M. Reece, Electric dipole moments in natural supersymmetry, J. High Energ. Phys. 8 (2017) 031.

[6] C. Cesarotti, Q. Lu, Y. Nakai, A. Parikh, and M. Reece, Interpreting the electron EDM constraint, J. High Energ. Phys. 5 (2019) 059.

[7] E. R. Meyer, J. L. Bohn, and M. P. Deskevich, Candidate molecular ions for an electron electric dipole moment experiment, Phys. Rev. A **73**, 062108 (2006).

[8] E. R. Meyer and J. L. Bohn, Prospects for an electron electric-dipole moment search in metastable ThO and Th F$^+$, Phys. Rev. A **78**, 010502(R) (2008).

[9] N. R. Hutzler, Polyatomic molecules as quantum sensors for fundamental physics, Quantum Sci. Technol. **5**, 044011 (2020).

[10] J. J. Hudson, D. M. Kara, I. J. Smallman, B. E. Sauer, M. R. Tarbutt, and E. A. Hinds, Improved measurement of the shape of the electron, Nature (London) **473**, 493 (2011).

[11] J. Baron *et al.* (ACME Collaboration), Order of magnitude smaller limit on the electric dipole moment of the electron, Science **343**, 269 (2014).

[12] V. Andreev *et al.* (ACME Collaboration), Improved limit on the electric dipole moment of the electron, Nature (London) **562**, 355 (2018).

[13] W. B. Cairncross, D. N. Gresh, M. Grau, K. C. Cossel, T. S. Roussy, Y. Ni, Y. Zhou, J. Ye, and E. A. Cornell, Precision Measurement of the Electron's Electric Dipole Moment Using Trapped Molecular Ions, Phys. Rev. Lett. **119**, 153001 (2017).

[14] D. E. Maison, L. V. Skripnikov, and V. V. Flambaum, Theoretical study of ^{173}YbOH to search for the nuclear magnetic quadrupole moment, Phys. Rev. A **100**, 032514 (2019).

[15] M. Denis, Y. Hao, E. Eliav, N. R. Hutzler, M. K. Nayak, R. G. E. Timmermans, and A. Borschesvky, Enhanced P, T-violating nuclear magnetic quadrupole moment effects in laser-coolable molecules, J. Chem. Phys. **152**, 084303 (2020).

[16] J. Lim, J. R. Almond, M. A. Trigatzis, J. A. Devlin, N. J. Fitch, B. E. Sauer, M. R. Tarbutt, and E. A. Hinds, Laser Cooled YbF Molecules for Measuring the Electron's Electric Dipole Moment, Phys. Rev. Lett. **120**, 123201 (2018).

[17] B. L. Augenbraun, Z. D. Lasner, A. Frenett, H. Sawaoka, C. Miller, T. C. Steimle, and J. M. Doyle, Laser-cooled polyatomic molecules for improved electron electric dipole moment searches, New J. Phys. **22**, 022003 (2020).

[18] I. Kozyryev and N. R. Hutzler, Precision Measurement of Time-Reversal Symmetry Violation with Laser-Cooled Polyatomic Molecules, Phys. Rev. Lett. **119**, 133002 (2017).

[19] T. A. Isaev, A. V. Zaitsevskii, and E. Eliav, Laser-coolable polyatomic molecules with heavy nuclei, J. Phys. B **50**, 225101 (2017).

[20] K. Gaul and R. Berger, *Ab initio* study of parity and time-reversal violation in laser-coolable triatomic molecules, Phys. Rev. A **101**, 012508 (2020).

[21] M. Denis, P. A. B. Haase, R. G. E. Timmermans, E. Eliav, N. R. Hutzler, and A. Borschevsky, Enhancement factor for the electric dipole moment of the electron in the BaOH and YbOH molecules, Phys. Rev. A **99**, 042512 (2019).

[22] S. Nakhate, T. C. Steimle, N. H. Pilgram, and N. R. Hutzler, The pure rotational spectrum of YbOH, Chem. Phys. Lett. **715**, 105 (2019).

[23] S. Eckel, P. Hamilton, E. Kirilov, H. W. Smith, and D. DeMille, Search for the electron electric dipole moment using Ω-doublet levels in PbO, Phys. Rev. A **87**, 052130 (2013).

[24] E. T. Mengesha, A. T. Le, T. C. Steimle, L. Cheng, C. Zhang, B. L. Augenbraun, Z. Lasner, and J. Doyle, Branching ratios, radiative lifetimes, and transition dipole moments for YbOH, J. Phys. Chem. A **124**, 3135 (2020).

[25] L. Chang (private communication) (2020).

[26] J. Baron *et al.* (ACME Collaboration), Methods, analysis, and the treatment of systematic errors for the electron electric dipole moment search in thorium monoxide, New J. Phys. **19**, 073029 (2017).

[27] J. Barry, D. McCarron, E. Norrgard, M. Steinecker, and D. DeMille, Magneto-optical trapping of a diatomic molecule, Nature (London) **512**, 286 (2014).

[28] S. Truppe, H. J. Williams, M. Hambach, L. Caldwell, N. J. Fitch, E. A. Hinds, B. E. Sauer, and M. R. Tarbutt, Molecules cooled below the Doppler limit, Nat. Phys. **13**, 1173 (2017).

[29] S. Ding, Y. Wu, I. A. Finneran, J. J. Burau, and J. Ye, Sub-Doppler Cooling and Compressed Trapping of YO Molecules at μK Temperatures, Phys. Rev. X **10**, 021049 (2020).

[30] D. Mitra, N. B. Vilas, C. Hallas, L. Anderegg, B. L. Augenbraun, L. Baum, C. Miller, S. Raval, and J. M. Doyle, Direct laser cooling of a symmetric top molecule, Science **369**, 1366 (2020).

[31] R. F. Wormsbecher and R. D. Suenram, Laser spectroscopy and chemiluminescence from the monomethoxides of Ca, Sr, and Ba, J. Mol. Spectrosc. **95**, 391 (1982).

[32] P. Crozet, F. Martin, A. Ross, C. Linton, M. Dick, and A. Adam, The $A^2E - X^2A_1$ system of $CaOCH_3$, J. Mol. Spectrosc. **213**, 28 (2002).

[33] D. Forthomme, C. Linton, A. G. Read, D. W. Tokaryk, A. G. Adam, L. E. Downie, A. D. Granger, and W. S. Hopkins, Unravelling the visible spectrum of strontium monomethoxide, J. Mol. Spectrosc. **270**, 108 (2011).

[34] L. C. O'Brien, C. R. Brazier, and P. F. Bernath, High-resolution laser spectroscopy of strontium monomethoxide, $SrOCH_3$, J. Mol. Spectrosc. **130**, 33 (1988).

[35] K. Namiki, J. Robinson, and T. Steimle, A spectroscopic study of $CaOCH_3$ using the pump/probe microwave and the molecular beam/optical Stark techniques, J. Chem. Phys. **109**, 5283 (1998).

[36] A. C. Paul, K. Sharma, M. A. Reza, H. Telfah, T. A. Miller, and J. Liu, Laser-induced fluorescence and dispersed-fluorescence spectroscopy of the $\tilde{A}^2E - \tilde{X}^2A_1$ transition of jet-cooled calcium methoxide (CaOCH3) radicals, J. Chem. Phys. **151**, 134303 (2019).

[37] C. R. Brazier, L. C. Ellingboe, S. Kinsey-Nielsen, and P. F. Bernath, Laser spectroscopy of alkaline earth monoalkoxide free radicals, J. Am. Chem. Soc. **108**, 2126 (1986).

[38] A. M. Ellis, Main group metal-ligand interactions in small molecules: New insights from laser spectroscopy, Int. Rev. Phys. Chem. **20**, 551 (2001).

[39] P. F. Bernath, Spectroscopy and photochemistry of polyatomic alkaline earth containing molecules, Adv. Photochem. **23**, 1 (1997).

[40] P. Crozet, A. J. Ross, C. Linton, A. G. Adam, W. S. Hopkins, and R. J. L. Roy, Geometry of the $CaOCH_3$ radical from isotope effects in the transition, J. Mol. Spectrosc. **229**, 224 (2005).

[41] B. L. Augenbraun, J. M. Doyle, T. Zelevinsky, and I. Kozyrev, Molecular Asymmetry and Optical Cycling: Laser Cooling Asymmetric Top Molecules, Phys. Rev. X **10**, 031022 (2020).

[42] I. Kozyrev, L. Baum, K. Matsuda, and J. M. Doyle, Proposal for laser cooling of complex polyatomic molecules, ChemPhysChem **17**, 3641 (2016).

[43] J. Lim, J. R. Almond, M. R. Tarbutt, D. T. Nguyen, and T. C. Steimle, The [557]-$X^2\Sigma^+$ and [561]-$X^2\Sigma^+$ bands of ytterbium fluoride, ^{174}YbF, J. Mol. Spectrosc. **338**, 81 (2017).

[44] T. C. Steimle, C. Linton, E. T. Mengesha, X. Bai, and A. T. Le, Field-free, Stark, and Zeeman spectroscopy of the $\tilde{A} - \tilde{X}$ transition of ytterbium monohydroxide, Phys. Rev. A **100**, 052509 (2019).

[45] N. J. Reilly, T. W. Schmidt, and S. H. Kable, Two-dimensional fluorescence (excitation/emission) spectroscopy as a probe of complex chemical environments, J. Phys. Chem. A **110**, 12355 (2006).

[46] J. R. Gascooke, U. N. Alexander, and W. D. Lawrance, Two dimensional laser induced fluorescence spectroscopy: A powerful technique for elucidating rovibronic structure in electronic transitions of polyatomic molecules, J. Chem. Phys. **134**, 184301 (2011).

[47] D. L. Kokkin, T. C. Steimle, and D. DeMille, Branching ratios and radiative lifetimes of the U, L, and I states of thorium oxide, Phys. Rev. A **90**, 062503 (2014).

[48] C. R. Brazier and P. F. Bernath, The $\tilde{A}^2E - \tilde{X}^2A_1$ transition of monomethyl calcium: A rotational analysis, J. Chem. Phys. **91**, 4548 (1989).

[49] A. J. Marr, F. Grieman, and T. C. Steimle, A molecular beam optical/Stark study of calcium monomethyl, J. Chem. Phys. **105**, 3930 (1996).

[50] I. J. Smallman, F. Wang, T. C. Steimle, M. R. Tarbutt, and E. A. Hinds, Radiative branching ratios for excited states of ^{174}YbF: Application to laser cooling, J. Mol. Spectrosc. **300**, 3 (2014).

[51] K. L. Dunfield, C. Linton, T. E. Clarke, J. McBride, A. G. Adam, and J. R. D. Peers, Laser spectroscopy of the lanthanide monofluorides: Analysis of the $\tilde{A}^2\Pi - \tilde{X}\Sigma^+$ transition of ytterbium monofluoride, J. Mol. Spectrosc. **174**, 433 (1995).

[52] T. C. Steimle, C. Linton, A. T. Le, and E. T. Mengesha, Spectroscopy of the YbOH $\tilde{A}^2\Pi_{3/2} - \tilde{X}^2\Sigma^+$ band, (unpublished).

[53] I. Kozyrev, T. C. Steimle, P. Yu, D.-T. Nguyen, and J. M. Doyle, Determination of CaOH and $CaOCH_3$ vibrational branching ratios for direct laser cooling and trapping, New J. Phys. **21**, 052002 (2019).

[54] A. Jadbabaie, N. H. Pilgram, J. Klos, S. Kotochigova, and N. R. Hutzler, Enhanced molecular yield from a cryogenic buffer gas beam source via excited state chemistry, New J. Phys. **22**, 022002 (2020).

[55] G. Herzberg, *Molecular Spectra and Molecular Structure* (Van Nostrand Reinhold, New York, 1950), Vol. 1.

[56] M. J. Dick, P. M. Sheridan, J.-G. Wang, and P. F. Bernath, High-resolution laser excitation spectroscopy of the $\tilde{A}^2E - \tilde{X}^2A_1$ transition of $SrCH_3$, J. Chem. Phys. **124**, 174309 (2006).

[57] G. Herzberg, *Molecular Spectra and Molecular Structure: Electronic Spectra and Electronic Structure of Polyatomic Molecules* (Van Nostrand, Princeton, NJ, 1966), Vol. 3.

[58] D.-T. Nguyen, T. C. Steimle, I. Kozyrev, M. Huang, and A. B. McCoy, Fluorescence branching ratios and magnetic tuning of the visible spectrum of SrOH, J. Mol. Spectrosc. **347**, 7 (2018).

[59] F. Neese, The ORCA program system, Wiley Interdiscip. Rev. Comput. Mol. Sci. **2**, 73 (2012).

[60] F. Neese, F. Wennmohs, U. Becker, and C. Riplinger, The ORCA quantum chemistry program package, J. Chem. Phys. **152**, 224108 (2020).

[61] D. Bykov, T. Petrenko, R. Izsák, S. Kossmann, U. Becker, E. Valeev, and F. Neese, Efficient implementation of the analytic second derivatives of Hartree-Fock and hybrid DFT energies: A detailed analysis of different approximations, Mol. Phys. **113**, 1961 (2015).

[62] P. J. Stephens, F. J. Devlin, C. F. Chabalowski, and M. J. Frisch, Ab initio calculation of vibrational absorption and circular dichroism spectra using density functional force fields, J. Phys. Chem. **98**, 11623 (1994).

[63] M. Dolg, H. Stoll, and H. Preuss, Energy-adjusted *ab intio* pseudopotentials for the rare earth elements, J. Chem. Phys. **90**, 1730 (1989).

[64] M. J. O'Rourke and N. R. Hutzler, Hypermetallic polar molecules for precision measurements, Phys. Rev. A **100**, 022502 (2019).

[65] T. A. Isaev and R. Berger, Polyatomic Candidates for Cooling of Molecules with Lasers from Simple Theoretical Concepts, Phys. Rev. Lett. **116**, 063006 (2016).

[66] B. E. Sauer, J. Wang, and E. A. Hinds, Laser-rf double resonance spectroscopy of ^{174}Yb in the $X^2\Sigma$ state: Spin-rotation, hyperfine interactions, and the electric dipole moment, J. Chem. Phys. **105**, 7412 (1996).

[67] B. E. Sauer, S. B. Cahn, M. G. Kozlov, G. D. Redgrave, and E. A. Hinds, Perturbed hyperfine doubling in the $A^2\Pi_{1/2}$ and [18.6]0.5 states of YbF, J. Chem. Phys. **110**, 8424 (1999).

[68] D. A. Weil and D. A. Dixon, Gas-phase isotope fractionation factor for proton-bound dimers of methoxide anions, J. Am. Chem. Soc. **107**, 6859 (1985).

[69] T. C. Steimle, T. Ma, and C. Linton, The hyperfine interaction in the $A\ ^2\Pi_{1/2}$ and $X\ ^2\Sigma^+$ states of ytterbium monofluoride, J. Chem. Phys. **127**, 234316 (2007).

[70] T. A. Barckholtz and T. A. Miller, Quantitative insights about molecules exhibiting Jahn-Teller and related effects, Int. Rev. Phys. Chem. **17**, 435 (1998).

[71] L. Baum, N. B. Vilas, C. Hallas, B. L. Augenbraun, S. Raval, D. Mitra, and J. M. Doyle, Establishing a highly closed cycling transition in a polyatomic molecule arXiv:2006.01769.

[72] V. S. Prasannaa, N. Shitara, A. Sakurai, M. Abe, and B. P. Das, Enhanced sensitivity of the electron electric dipole moment from YbOH: The role of theory, Phys. Rev. A **99**, 062502 (2019).

[73] K. M. O'Hara, S. R. Granade, M. E. Gehm, T. A. Savard, S. Bali, C. Freed, and J. E. Thomas, Ultrastable CO_2 Laser Trapping of Lithium Fermions, Phys. Rev. Lett. **82**, 4204 (1999).

[74] S. Bernon, H. Hattermann, D. Bothner, M. Knufinke, P. Weiss, F. Jessen, D. Cano, M. Kemmler, R. Kleiner, D. Koelle, and J. Fortágh, Manipulation and coherence of ultra-cold atoms on a superconducting atom chip, Nat. Commun. **4**, 2380 (2013).

[75] Y. Wang, M. Um, J. Zhang, S. An, M. Lyu, J.-N. Zhang, L.-M. Duan, D. Yum, and K. Kim, Single-qubit quantum memory exceeding ten-minute coherence time, Nat. Photonics **12**, 185 (2018).

[76] C. J. Ho, J. A. Devlin, I. M. Rabey, P. Yzombard, J. Lim, S. C. Wright, N. J. Fitch, E. A. Hinds, M. R. Tarbutt, and B. E. Sauer, New techniques for a measurement of the electron's electric dipole moment, New J. Phys. **22**, 053031 (2020).

[77] P. Yu and N. R. Hutzler, Probing Fundamental Symmetries of Deformed Nuclei in Symmetric Top Molecules, Phys. Rev. Lett. **126**, 023003 (2021).

[78] E. B. Norrgard, D. S. Barker, S. Eckel, J. A. Fedchak, N. N. Klimov, and J. Scherschligt, Nuclear-spin dependent parity violation in optically trapped polyatomic molecules, Commun. Phys. **2**, 77 (2019).

[79] Y. Hao, P. Navrátil, E. B. Norrgard, M. Iliaš, E. Eliav, R. G. E. Timmermans, V. V. Flambaum, and A. Borschevsky, Nuclear spin-dependent parity-violating effects in light polyatomic molecules, Phys. Rev. A **102**, 052828 (2020).

[80] K. Gaul, M. G. Kozlov, T. A. Isaev, and R. Berger, Chiral Molecules as Sensitive Probes for Direct Detection of p-odd Cosmic Fields, Phys. Rev. Lett. **125**, 123004 (2020).

[81] K. Gaul, M. G. Kozlov, T. A. Isaev, and R. Berger, Parity-nonconserving interactions of electrons in chiral molecules with cosmic fields, Phys. Rev. A **102**, 032816 (2020).

[82] C. E. Dickerson, H. Guo, A. J. Shin, B. L. Augenbraun, J. R. Caram, W. C. Campbell, and A. N. Alexandrova, Franck-Condon tuning of optical cycling centers by organic functionalization, arXiv:2010.04207.

[83] J. Zheng, X. Xu, and D. G. Truhlar, Minimally augmented Karlsruhe basis sets, Theor. Chem. Acc. **128**, 295 (2010).